Calibration and disparity maps for a depth camera based on a four-lens device

Cécile Riou
Bruno Colicchio
Jean Philippe Lauffenburger
Olivier Haeberlé
Christophe Cudel

Calibration and disparity maps for a depth camera based on a four-lens device

Cécile Riou, Bruno Colicchio, Jean Philippe Lauffenburger, Olivier Haeberlé, and Christophe Cudel*
Université de Haute Alsace, Laboratoire MIPS (EA2332), 61 rue Albert Camus, Mulhouse 68093, France

Abstract. We propose a model of depth camera based on a four-lens device. This device is used for validating alternate approaches for calibrating multiview cameras and also for computing disparity or depth images. The calibration method arises from previous works, where principles of variable homography were extended for three-dimensional (3-D) measurement. Here, calibration is performed between two contiguous views obtained on the same image sensor. This approach leads us to propose a new approach for simplifying calibration by using the properties of the variable homography. Here, the second part addresses new principles for obtaining disparity images without any matching. A fast algorithm using a contour propagation algorithm is proposed without requiring structured or random pattern projection. These principles are proposed in a framework of quality control by vision, for inspection in natural illumination. By preserving scene photometry, some other standard controls, as for example calipers, shape recognition, or barcode reading, can be done conjointly with 3-D measurements. Approaches presented here are evaluated. First, we show that rapid calibration is relevant for devices mounted with multiple lenses. Second, synthetic and real experimentations validate our method for computing depth images. © 2015 SPIE and IS&T [DOI: 10.1117/1.JEI.24.6.061108]

1 Introduction

Multiview imaging is a large domain, where numerous approaches can take place for computing the depths in a scene. Stereovision,[1] multicamera array,[2] light-field imaging,[3,4] and coded aperture imaging[5] are the best-known techniques for capturing several point of views of a scene. Using a metric calibration on these systems allows for addressing recently growing applications in a research or industrial context. In multiview imaging, the depth estimation problem is then related to the disparity between same pixels projected on the different coordinates in the different views. This task usually relies on the identification of the similarity between the different views, allowing for computing displacements of identified points and their corresponding three-dimensional (3-D) positions. The similarities identification is usually a time-consuming task and is referenced as matching methods based on local or global methods.[6] Local methods compare two regions of interest by measuring similarity with well-known criteria such as block matching or feature approaches.[7] These approaches are efficient on images containing a large percentage of textured area, but fail for uniform regions, because these areas contain too few information for the matching process. Occluded regions, due to the difference of point of views, are another cause of occurring errors in the matching process. Global approaches can overcome some of these issues, by estimating a disparity map that minimizes energy criteria on the whole image. Graph cuts,[8] belief propagation,[9] and dynamic programming[10] methods are the best-known global approaches. Computational complexity of these methods is often high,
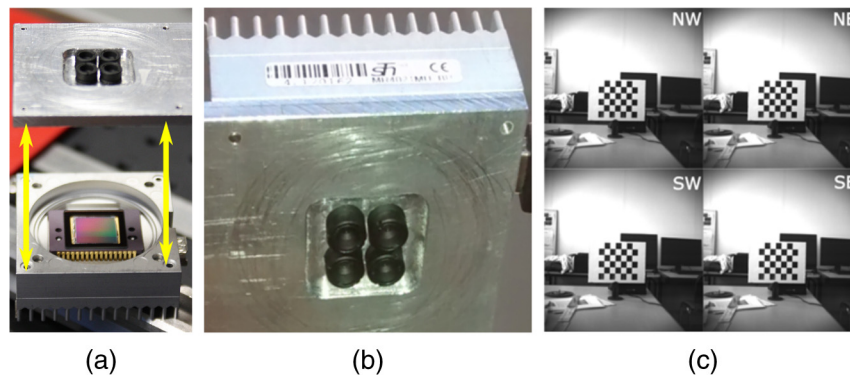
and they are not able to properly solve the cases where images contain large uniform surfaces. For robotics or industrial control, light patterns are projected on whole objects and background of the scene, for helping the matching process. In this case, patterns modify the aspect of homogeneous objects, which seem to be textured. These active techniques are efficient for computing disparity map, but images are then unusable for any other controls such as edge detections, intensity measurements, barcode reading, or optical character recognition (OCR).

In order to deduce a depth from disparity, a metric calibration of the acquisition system is needed. Usually, calibration consists of determining intrinsic parameters for the acquisition device used for metric measurements and permits to compute distances between scene objects and the camera device. An interesting survey of the reference methods is proposed by Zhang,[11] where approaches are divided into three categories following the reference object used for calibration. Highest accuracy can theoretically be obtained by using a 3-D object for calibration, but in practice, calibration with a two-dimensional (2-D) apparatus seems to be the best choice in most situations, because of its ease of use and good accuracy. In this case, calibration is performed by taking images of the 2-D pattern plane under different orientations by moving either the plane or the camera. A dozen of acquisitions are then a recommended minimum. Calibration of multicamera devices has been studied by Vaish et al.[2] This work compares a nonmetric approach, using plane and parallax, with metric calibration for computing synthetic aperture images. If the operating mode for calibrating is similar to our approach developed in this paper, the proposed

*Address all correspondence to: Christophe Cudel, E-mail: christophe.cudel@uha.fr

affine model leads to generate images focused at different relative or uncalibrated depths.

We propose in this work a multilens device (Fig. 1) and a postprocessing algorithm using contours in order to avoid computing a disparity map of homogeneous objects by using projected light patterns. A fast and flexible calibration step is also proposed. The calibration of this device could be qualified as an indirect method, because intrinsic parameters are not determined individually as is usually done, but in an overall manner using a reference homography. One of the main interests is to simplify the calibration step, which is then easily achievable by an operator for industrial applications. This method is an improvement of previous works,[12] in which we have extended the principles of "variable homography," defined by Zhang and Greenspan[13] for measuring the height of emergent fibers on glass and nonwoven fabrics. This method has been defined for working with fabric samples progressing on a conveyor belt. Triggered acquisition of two successive images was needed to perform 3-D measurements. In this work, we have retained advantages of variable homography for measurements along the optical axis, but we have reduced the acquisitions to a unique one, by developing a device made of four lenses placed in front of a single-image sensor. We have also adapted the variable homography formulation for this device, and we give a new formulation to calculate the depth. This method is presented in the first part of this paper and can be applied to any disparity maps calculated from various methods. In the second part, we propose also a new framework for computing disparity map adapted to our device, which then becomes a depth camera. The disparity map computation is an alternate to matching methods, exploring a contour-based solution, where no correspondence matching is needed, drastically reducing the computational time. In 3-D industrial control by vision, most of stereovision systems project structured or random patterns on objects for providing texture on uniform surfaces. This method is efficient for measuring disparities between the multiple views, but in this case, only the depth images can be used for image analysis because the scene photometry is strongly modified by the projected pattern. On the contrary, we propose an algorithm preserving gray-image levels. The camera could then be used to both measure object height and perform any other classic vision control, such as optical character or pattern recognition. However, this method is not fully universal, and we have only studied cases for measuring flat objects, in a context of industrial control.

This paper presents first the geometry of our device and describes the extension of variable homography for 3-D measurements. This approach leads to propose a new calibration scheme, for which only a reference homography is needed, instead of the intrinsic parameters, as usually. Second, we have proposed an alternate manner of computing a depth map. Preliminary and promising results on synthetic and real images are presented in the last part.

2 Variable Homography and Depth Measurements from Disparity

The concept of variable homography has been defined by Zhang and Greenspan[13] for parallax compensation in image mosaicking without metric calibration. This concept has then been extended by Xu et al.[12] for 3-D measurements by using two successive acquisitions of fabrics scrolling on a conveyor belt.

This part presents how the variable homography can be used for modeling our multiview device, described in Fig. 1. Figure 2 gives a schematic representation of our
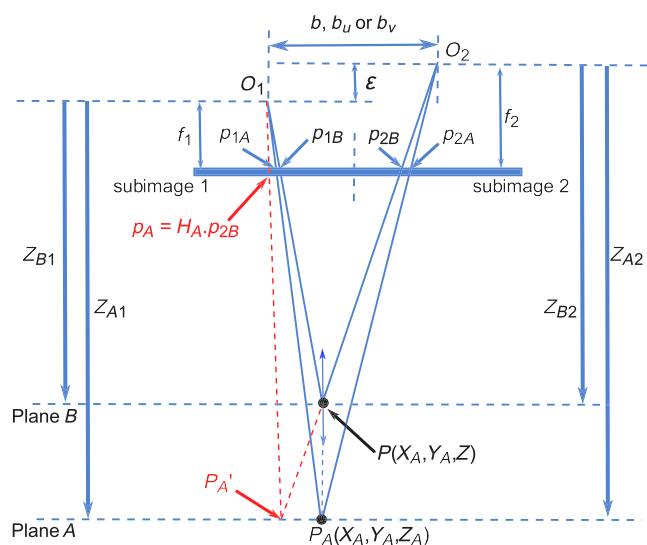
Fig. 2 Geometric cross-section between two adjacent subimages. O_1, O_2: optical centers of subimages 1 and 2; b: distance between O_1 and O_2; f_1, f_2: lenses focal distances; ε: difference between f_1 and f_2; Z_{Ai}, Z_{Bi}: distances between O_i and planes A and B; p_{1A} and p_{2A}: P_A projections on both subimages; p_{1B} and p_{2B}: P projections on both subimages; and p_A: projection on subimage 1 of the virtual point P'_A.

Fig. 1 (a) Exploded view of the camera with its four minilenses, (b) assembled camera, and (c) corresponding subimages (NW, north-west, NE, north-east, SW, south-west, and SE, south-east).

system made out of minilenses and a single-image plane. This figure is a 2-D section representing only two neighboring projections, given the subimages noted I_i and I_{i+1} (we will use $I = 1$ for next equations). With four projections on the image sensor, each subimage has three possible neighbors. If index i represents the SE view (south-east), index $I + 1$ can be any view of NE (north-east), SW (south-west), or NW (north-west). This scheme simplifies our system to a parallel stereovision system, where triangulation could be used to determine the depth of point P when intrinsic and distortion parameters are known. Ideal situation is encountered when these parameters are identical for each camera, which is however never the case in practice. Precise calibration is then needed to determine numerical values of optical centers and focal distances. These parameters are necessary for the geometric reprojection, for computing depth by intersecting the two rays of each associated left and right image pixels. For example, in Fig. 2, f_1, f_2, O_1, and O_2 must be known for recovering the depth of a point P from the rays $(O_1\ p_{1B})$ and $(O_2\ p_{2B})$.

An alternative approach is to take benefit of variable homography for modeling this device.

2.1 Variable Homography Definition for a Pair of Views

Variable homography formulation introduces a matrix K giving some interesting properties between both homographies H_A and H_B defined for the A and B parallel planes and verifying $p_{1A} = H_A \cdot p_{2A}$ and $p_{1B} = H_B \cdot p_{2B}$:

$$H_B(k) = K_i \cdot H_A \cdot K_{i+1}^{-1}$$
$$\text{where } K_n = \begin{bmatrix} k_n & 0 & (1-k_n)u_{0n} \\ 0 & k_n & (1-k_n)v_{0n} \\ 0 & 0 & 1 \end{bmatrix}, \quad (1)$$

with $n = i$ or $i + 1$ and where u_{0n} and v_{0n} stand for the coordinates of the optical centers O_n projected on the image sensor. The main parameter of K is the distance ratio k_n defined by $k_n = Z_{An}/Z_{Bn}$, giving the possibilities to compute H_B from H_A. By sweeping k around realistic values and by using a matching comparison method, it would be possible to find reliable correspondences where $k = \text{argmax}\{\text{Matching}[p_{1B}(k), p_{2B}]\}$. This is the idea presented by Zhang and Greenspan[13] in their paper to compensate parallax in image mosaicking. We propose to extend this method, by developing the equations of H_A and H_B, in order to simplify the reprojection equation to compute depth and easily include in our model all intrinsic parameters described in Fig. 2.

2.2 H_A and H_B Equations

Plane A is considered as the reference plane and is used for calibrating the device. As our device uses four minilenses, it is interesting to study the case where these lenses do not have exactly the same focal distances. H_A is then determined by assuming that homography is a combination of an intrinsic parameter and translation matrices and is given in Ref. 1 as

$$H_A = \begin{pmatrix} \frac{f_1}{f_2}\frac{Z_{A2}}{Z_{A1}} & 0 & u_{01} + \frac{b_u f_1}{Z_{A1}} - \frac{f_1}{f_2}\frac{Z_{A2}}{Z_{A1}}u_{02} \\ 0 & \frac{f_1}{f_2}\frac{Z_{A2}}{Z_{A1}} & v_{01} + \frac{b_v f_1}{Z_{A1}} - \frac{f_1}{f_2}\frac{Z_{A2}}{Z_{A1}}v_{02} \\ 0 & 0 & 1 \end{pmatrix}$$

$$= \begin{pmatrix} \alpha & 0 & u_{01} + \frac{b_u f_1}{Z_{A1}} - \alpha \cdot u_{02} \\ 0 & \alpha & v_{01} + \frac{b_v f_1}{Z_{A1}} - \alpha \cdot v_{02} \\ 0 & 0 & 1 \end{pmatrix}, \quad (2)$$

where b_u and b_v are the horizontal and vertical distances between optical centers, respectively. By considering $Z_{A2} = Z_{A1} + \varepsilon \approx Z_{A1}$ at the working distances, H_A has been simplified in Eq. (2) by introducing the focal distance ratio $\alpha = f_1/f_2$. Equations (1) and (2) lead to give a simplified equation for H_B, representing the geometric transformation for any point P located in a virtual plane B, parallel to the reference plane A:

$$H_B = \begin{pmatrix} \alpha & 0 & u_{01} + k_1\frac{b_u f_1}{Z_{A1}} - \alpha \cdot u_{02} \\ 0 & \alpha & v_{01} + k_1\frac{b_v f_1}{Z_{A1}} - \alpha \cdot v_{02} \\ 0 & 0 & 1 \end{pmatrix}. \quad (3)$$

2.3 Point P Depth Computation from a Pair of Views

From H_A and H_B homographies, we propose to compute the depth of any point P, by the definition of disparity d given by $d = H_B \cdot p_{2B} - H_A \cdot p_{2B}$. By considering that $p_{1B} = H_B \cdot p_{2B}$ and with Eqs. (2) and (3), d can be written as

$$d = \underbrace{H_B \cdot p_{2B}}_{p_{1B}} - \underbrace{H_A \cdot p_{2B}}_{p_A} = \text{dist}(p_{1B}, p_A)$$

$$= \left\{ \left[\underbrace{(k_1 - 1)\overbrace{\frac{b_u f_1}{Z_{A1}}}^{C_u}}_{d_u} \right]^2 + \left[\underbrace{(k_1 - 1)\overbrace{\frac{b_v f_1}{Z_{A1}}}^{C_v}}_{d_v} \right]^2 \right\}^{1/2}. \quad (4)$$

Assuming that $k_1 = Z_{A1}/Z_{B1}$ and $b = \sqrt{b_u^2 + b_v^2}$, relations between depth Z_{B1} and disparity d are finally given by

$$Z_{B1} = Z_{A1}\frac{\sqrt{C_u^2 + C_v^2}}{d \cdot Z_{A1} + \sqrt{C_u^2 + C_v^2}} = \frac{bf_1}{d + \frac{bf_1}{Z_{A1}}} \quad \text{or}$$

$$d = \frac{bf_1}{Z_{B1}} - \frac{bf_1}{Z_{A1}}. \quad (5)$$

This definition of disparity is slightly different from the one usually given. In the next part, we study the differences and advantages to use this definition for 3-D measurements, especially in a 3-D industrial vision context.

2.4 Comparison with Triangulation Method

When two cameras are separated by lateral translation with no rotation, triangulation method leads to obtain the depth relative to p_{1B} and p_{2B} coordinates. From Fig. 2, depth Z_{B1} can be expressed as

$$Z_{B1} = \frac{b + \frac{\varepsilon}{f_2}(O_2 - p_{2B})}{\frac{(p_{2B} - O_2)}{f_2} - \frac{(p_{1B} - O_1)}{f_1}}. \tag{6}$$

This relation is usually simplified assuming $f_1 = f_2$ and $O_1 = O_2$ in the coordinate systems of each subimage:

$$Z_{B1} = \frac{bf_1}{d} \quad \text{with } d = p_{2B} - p_{1B}. \tag{7}$$

By comparing this equation with the one obtained with variable homography, there is an evident similarity, and variable homography translates the disparity d by a term of $(-bf_1/Z_{A1})$. This is observed in Fig. 3, comparing Eqs. (7) and (5). Curves are plotted according to the real dimensions of our device: pixels size of 10 μm, optical centers spaced by 9 mm, and $f_1 = f_2 = 8$ mm. Triangulation curve is plotted in red, and the ones obtained from Eq. (5) are plotted in blue for several values of the reference distance Z_{A1}. In function of Z_{A1}, blue curves are thus shifted to the left. In fact, this translation offers some interesting properties. When the range of measurement is predicable, it would then be possible to work in the same range of disparity whatever the working depth, by choosing correctly Z_{A1}.

It is quite easy to demonstrate that the depth error ∂Z_{B1} stays identical for both approaches, meaning this translation does not influence the accuracy of measurement:

$$\frac{\partial d}{\partial Z_{B1}} = -\frac{bf_1}{Z_{B1}^2} \rightarrow \partial Z_{B1} = -\frac{Z_{B1}^2}{bf_1} \partial d. \tag{8}$$

There are some advantages to use variable homography for working within the same range of disparity. The same device and same algorithm can be used for a wide-working distance range, from macroscopic applications to higher scales. For example, if Z_{A1} equals 7 cm, depth Z_{B1} is ranged between 7 and 5.8 cm for an interval of d of [0,20] pixels. For 3-D industrial vision inspection, when Z_{A1} is fixed at 90 cm, the corresponding measured depths are ranged from 90 to 26 cm, while keeping the same d interval. We can note
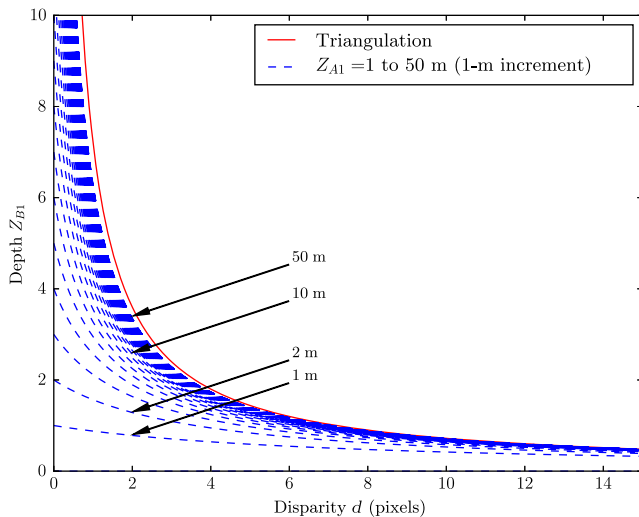
Fig. 3 Depths Z_{B1} function of disparity d. Triangulation and variable homography comparison.

that, for these different scales of measurements, we have used the same device. Switching between the different scales only requires adjusting the lenses focal distances. This last point is important, because in this case, accurate measurement would need to redetermine all intrinsic parameters using Eq. (6) when triangulation method is used. Next part explains how variable homography leads to an easier calibration step.

2.5 Simplified Calibration for Multiview Cameras

In practice, lenses are never perfectly aligned in multilens cameras (lenses are not sorted), and lens focal distances are also never strictly equal.[14] This is especially true for our prototype and this creates some undesirable distortions affecting depth measurements. In practice, imperfections are rarely taken into account and literature usually gives Eq. (7) as reference method to compute depth instead of the complete equation given by Eq. (6). By considering a multiview device, the complete determination of these intrinsic parameters could be an uncomfortable task, requiring multiple acquisitions,[15] but nevertheless mandatory for providing accurate measurements.

A great advantage of variable homography is to include in matrix H_A all intrinsic parameters between the views of two subimages. By projecting measurement points from subimage 2 to subimage 1 with H_A, the number of required parameters for 3-D measurement is then reduced, and they are easy to determine via a simple calibration process. Sole parameters to recover during the calibration step are: Z_{A1}, H_A, and the constant bf_1. The easy and robust proposed calibration method is realized by using a reference chessboard pattern for detecting corners and by performing two successive acquisitions. The first acquisition is done at reference depth Z_{A1}, and the second one at depth $Z_{B1} = Z_{A1} + d_z$. Corners of first acquisition are used to calculate all combinations of existing H_A homographies between subimages. For each acquisition, distances in pixels between the first and last corners detected on the chessboard are computed. We note d_A, the distance for the dataset of first acquisition and d_B, the distance for dataset of the second one. Z_{A1} is then obtained by triangulation and is formulated as

$$Z_{A1} = \frac{d_z \cdot d_B}{d_B - d_A}. \tag{9}$$

Finally, Z_{A1}, H_A, d_z, and distances d, computed for corresponding corners p_{1B} and p_{2B} during the second acquisition, lead to find the best value for bf_1. In conclusion, interest of this calibration lies in its simplicity when calibrating, because it is easier to calibrate via two acquisitions than to determine the intrinsic parameters with several snap images, as usually done with well-known standard methods.[15]

This calibration process for determining the variable homography parameters has been established by considering two views. This principle is easily extensible for a n-view camera, i.e., our device. Calibration is then performed for each pair of working views, without additional acquisition.

2.6 Improved Calibration with Lens Distortion Correction

Our multiview camera prototype uses low-cost lenses, presenting a distortion coefficient close to 1.5% (value is issued from lens datasheet). To improve measurements accuracy, we propose to take into account the distortion in our calibration scheme. By using standard approaches, such as corrections by using radial distortion models, the precise positions of the optic centers of each subimage can be determined. As these intrinsic parameters are combined in H_A, they are not immediately available at this step with our calibration process. We propose therefore an alternate approach. We consider that the distortion effects are comparable with a nonuniform image magnification on image plane. This approach leads to adjust the computation of Z_{B1} as a function of the spatial location of correspondences in subimages. This can be done by using the proportional relationship existing between magnification, focal distance, and parameter bf_1. The correction is performed by using the Γ operator, which transforms a vector representing a point P of coordinates $(u, v, 1)$ in the lifted coordinates[16] $\tilde{P}$:

$$P(u,v,1)^T \rightarrow \tilde{P} = \Gamma(P,P) = (u^2, v^2, u \cdot v, u, v, 1)^T. \quad (10)$$

By using p_{B1} as reference location, bf_1 is then computed by the quadratic functions defined by

$$bf_1 = \begin{pmatrix} a & b & c & d & e & f \end{pmatrix} \cdot \tilde{p}_{B2}. \quad (11)$$

Corners collected previously form a dataset and permit computation of the polynomial coefficients by using a least mean square method.

2.7 Measurement Accuracy

The measurements obtained in this part have been obtained with our device presenting the following characteristics: CCD size: 15×15 mm^2; CCD resolution: 2048×2048 pixels; minilenses diameters: 8 mm; minilenses focal distance: 7.5 mm; distance between minilenses: 9 mm; and subimages resolution: 550×550 pixels. We present experimental measurements for three ranges of depth, in order to estimate the accuracy of our device in term of depth measurement. Here, only measurements performed on SW and SE subimages are presented for this experimentation. As shown by Eq. (8), depth error is a function of two factors: geometric parameters estimation and disparity measurement.

At this point, we are interested in measuring the quality of the parameters estimated during calibration. For minimizing the role of disparity measurement in our estimation, we have used a pattern chessboard as depth target and corners detection is performed with the corresponding function of the OpenCV library. For each depth level, numerous acquisitions are performed, leading to about 1000 measurements. We have set the camera-chessboards distances at 4, 33 and
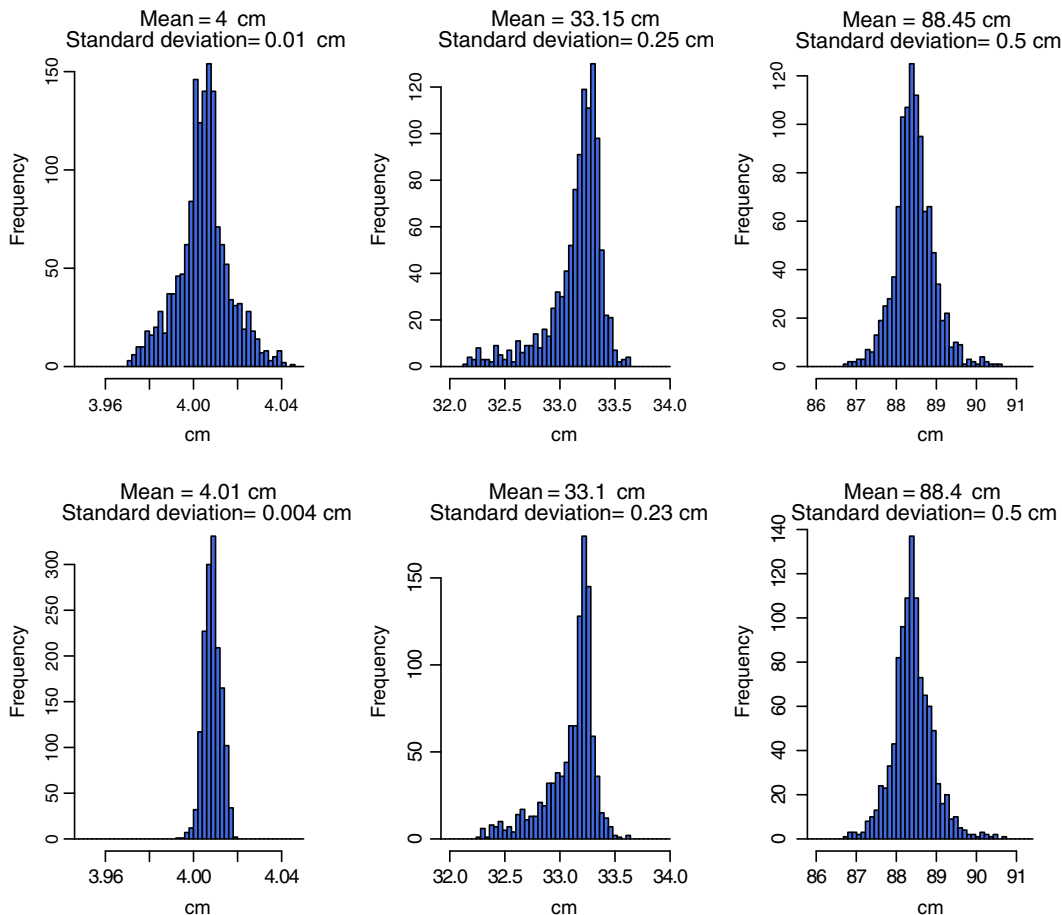

Fig. 4 Depth measurement distributions for three ranges of measurements: 4, 33, and 88.5 cm. Top: results of simplified calibration method; and bottom: results of improved calibration method.

88.5 cm, and the measured depth corresponds to Z_{B1} (distance separating the chessboard and the optical center). Figure 4 gives the distributions of depth measured for each corner. By working at a short distance, captured images present important optical distortions. In this case, the second method offers a significant improvement, providing a standard deviation lower than 1%. For evaluating depth error, percentage is not significant here, because the uncertainty of measurements is directly linked to the depth range [see Eq. (8)], meaning depth error increases systematically with depth.

This is the reason why our evaluation is presented by comparing theoretically predicted error with the measured standard deviation. In this case, the main difficulty concerns evaluation of the disparity variation ∂d, which is a difficult to assess parameter. Even if we use a subpixel corner detector, ∂d heavily depends on the pattern chessboard scale in subimages and thus of the working distance. To provide the best estimations, we have bounded its values between two realistic limit values, fixed here at 0.1 and 0.5 pixels. These values are then used for the result comparisons presented in Table 1. This table shows that the standard deviations observed during our measurements are comprised within the range of estimated depth error. This confirms that the proposed calibration is well adapted to our measurement approach by variable homography. These values of depth error allow for keeping a good uncertainty of measurements for applications in the field of metrology by vision.

2.8 Subimage Rectifications

Previous measurements were performed on coordinates of detected corners. To transform our device into a depth camera, disparity has to be computed on all pixels of the subimage. As we have defined disparity as $d = p_{1B} - H_A \cdot p_{2B}$, a simple preprocessing steps can be performed, for rectifying each subimage with homography H_A. In this case, a reference subimage must be chosen. Next examples consider SE as reference subimage, as illustrated in Fig. 5, but any other subimage could be selected instead. By rectifying subimages, we ensure that correspondences between images are well aligned along the epipolar line, as is well known in stereovision. By organizing lens positions in a square, epipolar lines are then horizontal, vertical, or diagonal following positions of subimages used for computing disparity. Multiview approach is then interesting because in the reference subimage, epipolar lines calculated from other views could be combined to improve the matching for establishing correspondences and thus enhanced the final disparity map.
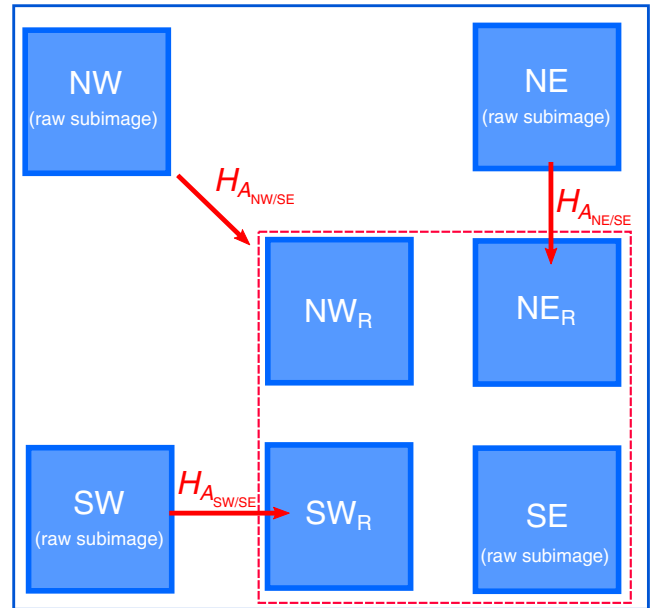
Fig. 5 Subimage rectification: preprocessing before computing disparity maps. By choosing SE as reference subimage, disparity maps between (SE, SW_R), (SE, NE_R), and (SE, SE_R) can be computed.

3 Computation of Disparity with the Four Minilens Device

With the set of rectified images, we propose to compute the corresponding disparity image (or disparity map), in order to use our device as a depth camera. The main idea is to subtract distances map between subimages in order to highlight the disparity values. This approach is to be used in a normal lightning environment with uniform objects. The next section shows that the proposed method does not need complex calculations, which is an advantage for real-time applications. However, this method is not universal, and can, up to now, be used for flat objects only.

3.1 Principle

The four subimages delivered by our device can be combined for computing up to three disparity images. We have validated the principle by using only two associations with three subimages: disparity (SE, SW_R) and disparity (SE, NE_R). The reference subimage is then SE, as illustrated in Fig. 5. Our goal is to fill the content of any objects by the disparity existing between comparable contours of two

Table 1 Comparison between theoretical and experimental depth measurement errors ($bf_1 = 7.2$ pixels is obtained during the calibration stage).

Depth Z_{B1} (cm)	Predicted depth error $\partial Z = (z^2/bf_1) \cdot \partial d$	Range of estimated theoretical depth error		Observed experimental standard deviation (SC/IC) (mm)
		$\partial d_{min} = 0.1$ pixel (mm)	$\partial d_{max} = 0.5$ pixel (mm)	
4	$(0.22 \times 10^{-3}) \cdot \partial d = 0.05$ mm	0.022	0.111	0.12/0.04
33	$(15.1 \times 10^{-3}) \cdot \partial d = 3.78$ mm	1.51	7.56	2.47/2.29
88.5	$(107 \times 10^{-3}) \cdot \partial d = 2.69$ cm	10.7	53.8	49.6/50.1

Note: SC: simplified calibration; IC: Improved calibration.

subimages. To do so, we propose an algorithm composed of four main steps and operating between two subimages:

- computation of distance images DI^{xx};
- computation of pseudo-subtraction images pSI^{xx};
- application of a fusion process; and
- computation of a disparity map by decoding the image given in the previous step.

As up to three disparity maps can be computed from the reference subimage, a second and final step merges these maps in order to eliminate some artifacts. The depth image is then directly obtained, thanks to the previous calibration, and using Eq. (5).

3.1.1 *Distance images: DI^{xx}*

The first step generates distance images (DI) following predetermined directions. When the working subimages are horizontals, then DI^{LR} (distance image left to right) and DI^{RL} (distance image right to left) are generated. Similarly, top/bottom distance images are generated when working subimages are vertical. Diagonal extension is also possible. Distance images are constituted of values indicating the distances between pixels to the previous contour encountered following the scanning direction. A flag $\times$ is used when no contour has been yet encountered by scanning. Figure 6 illustrates the examples to compute DI^{LR} and DI^{RL} images from SE and SW_R views. On this example, a rectangular object is represented by its contour pixels. A disparity d (or parallax d_u) of four pixels is simulated and the green points P_1 and P_2 represent a point having same coordinates on both original subimages. The main property used for our method is based on the fact that the difference $DI^{LR}(SE) - DI^{LR}(SW_R)$ or $DI^{RL}(SE) - DI^{RL}(SW_R)$ for any pixel inside the object is a function of the disparity value d.

3.1.2 *Pseudo-subtraction image: pSI^{xx}*

We have defined two distinct operators for exploiting the property that subtraction between DI images can give the disparity. Furthermore, this property is not true on the whole image, especially when the flag $\times$ is encountered. We have established that the best result, where object is filled by the disparity value, is obtained by using two kinds of subtraction called here pseudo-subtraction, where the result

value can be the flag $\times$, the first operand or the true difference. These operators are defined with arguments a and b, where a and b are the pixel values of the reference image and the second input image, respectively. Definitions of these operators are for DI^{LR} images:

$$pSI^{LR}(a, b) \rightarrow \begin{cases} (a - b) & \text{if } a, b \in N \\ \times & \text{otherwise} \end{cases}, \quad (12)$$

and for DI^{RL} images

$$pSI^{RL}(a, b) \rightarrow \begin{cases} (a - b) & \text{if } a, b \in N \\ a & \text{if } b = \times \\ \times & \text{otherwise} \end{cases}. \quad (13)$$

3.1.3 *Fusion image*

The fusion uses pSI^{LR} and pSI^{RL} images for replacing on pSI^{LR} image, the values appearing outside object by flag $\times$. This operation is simply defined by

$$FI(a, b) \rightarrow \begin{cases} a & \text{if } a, b \in N \\ \times & \text{otherwise} \end{cases}. \quad (14)$$

3.1.4 *Decoded fusion image*

The goal of this final step is to decode the content of fusion image in order to identify each object by its disparity, position, and dimension. Thanks to the previous steps, especially the distance propagation and pseudo-subtraction ones, a complete description of objects contained in original subimages can be extracted from the pixel values of the fusion image. These values are constituted of combinations of objects positions, sizes, and disparities. For N separated objects in each view, we have established by simulations that each pixel value in fusion image can be decoded. We note and define:

- d_i, l_i, and p_i, respectively, the disparity, length, and first position of object i;
- $A_i = -d_i$; $B_i = l_i$-d_i-1; $C_i = p_i$-d_i-p_{i-1}-l_{i-1} + 1;
- $Seq_1 = |A_1 \ldots A_1 B_1 \ldots B_1 A_1 \ldots A_1|$; and
- $Seq_i = |C_i \ldots C_i A_i \ldots A_i B_i \ldots B_i A_i \ldots A_i|$.
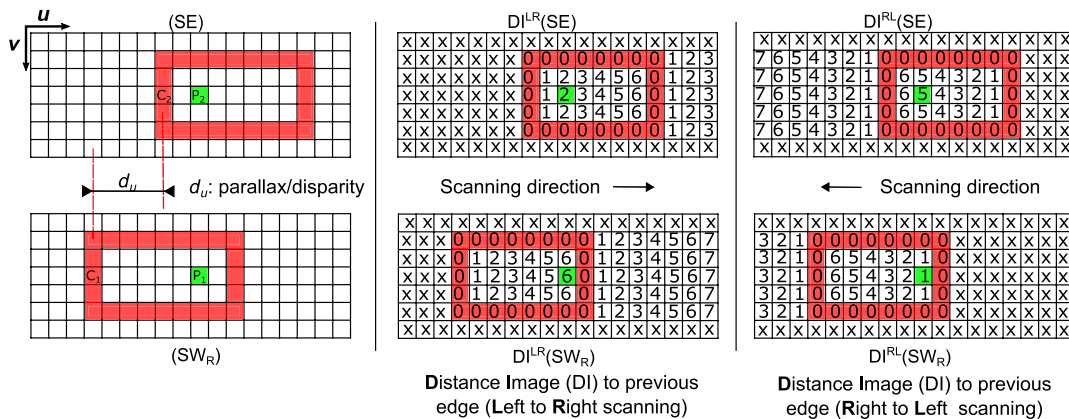

Fig. 6 Example of computation of distance image DI^{LR} and DI^{RL}.

Each line of the fusion image is then constituted of the following typical sequences arrangement: $[\times \ldots \times; Seq_1; Seq_2; \ldots Seq_i; \ldots Seq_N; \times \ldots \times]$. The number of occurrences of terms A_i, B_i, and C_i inside each sequence depends on the disparity, length, and position of objects in the subimages. This information is not used for the decoding. For example in Fig. 7, with $d_1 = 4$ and $l_1 = 8$, where image fusion is constituted of the arrangement $[\times \ldots \times; -4; -4; -4; 3; 3; 3; 3; -4; \times \ldots \times]$, one can recognize Seq_1.

Finally, the role of the decoding stage is to use this property for producing the disparity map. Depth images are then established with Eq. (5), linking depth and disparity.

3.2 Merging Disparity Maps

The algorithm presented above computes disparity map from two subimages. A complete overview, resuming step connections, is shown in Fig. 8. This scheme is designed to work with any couple of subimages. As this approach is only based on the contours detected in each subimage, the quality of initial contours is a primary initial prepreprocessing step. For the moment, no matching process is performed between subimages and this is an advantage of this approach. Even if matching could be useful for ensuring that each contour

point in subimage i would have a corresponding point in subimage $i + 1$, we have decided to skip it, for increasing the speed of our method. But, with no matching process, some contours in subimage i may have no correspondence in subimage $i + 1$. DI images are then affected and some artifacts in disparity images can appear. Following scanning direction, they are characterized by horizontal, diagonal, or vertical trails. A solution for attenuating these artifacts has been found by exploiting the multiview capability of our device. As from a reference image (see Fig. 5), three disparity maps can be computed, we propose to merge them for smoothing artifacts and retaining the most plausible disparity value for each pixel.

3.3 Results

Figure 9 presents some results on synthetic scenes, showing objects located at several depths. The first case shows a basic configuration, where objects are located far away from each other. A second case shows superimposed objects. For these two cases, no final merging is necessary and only one disparity map is sufficient to generate the final depth image. For the last example, we consider a situation where all contours pixels have no correspondences in subimages, as can happen
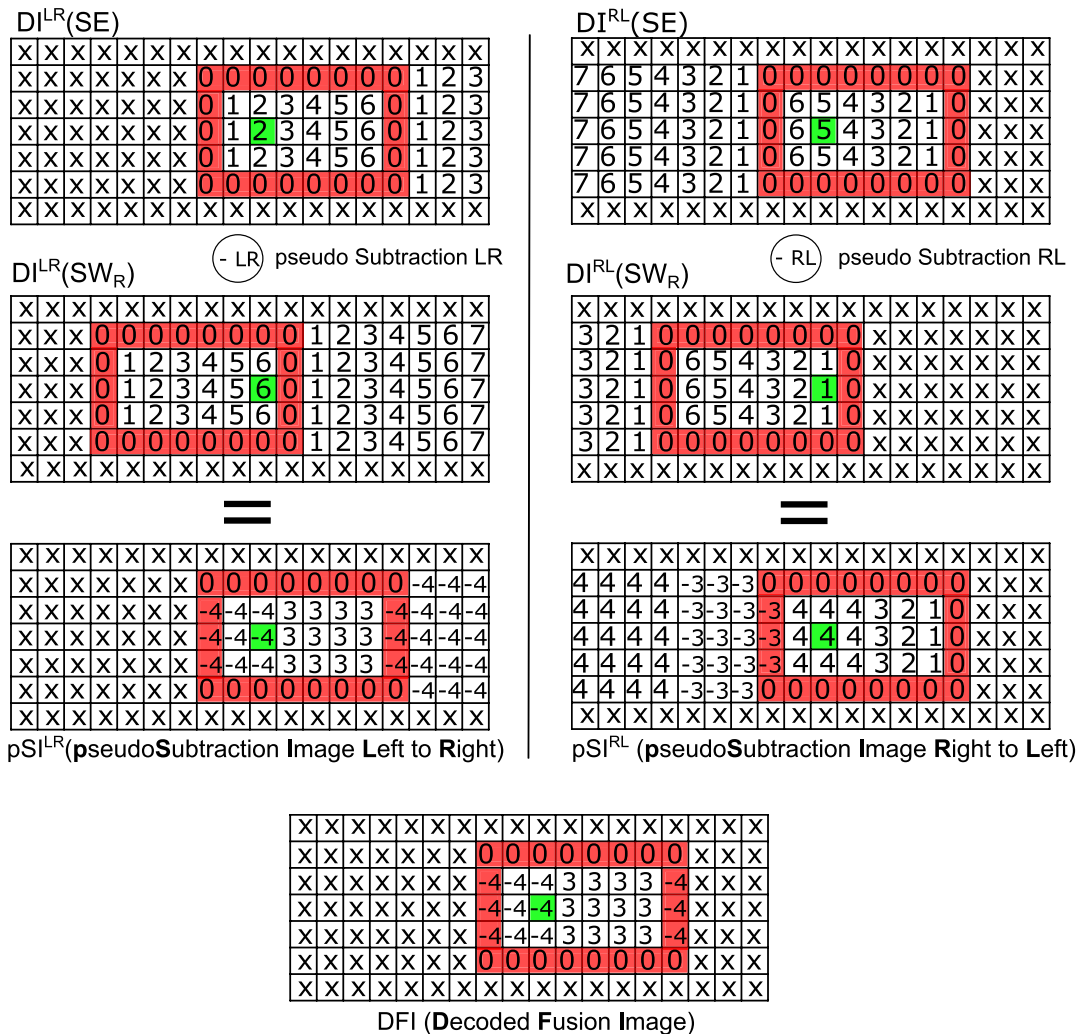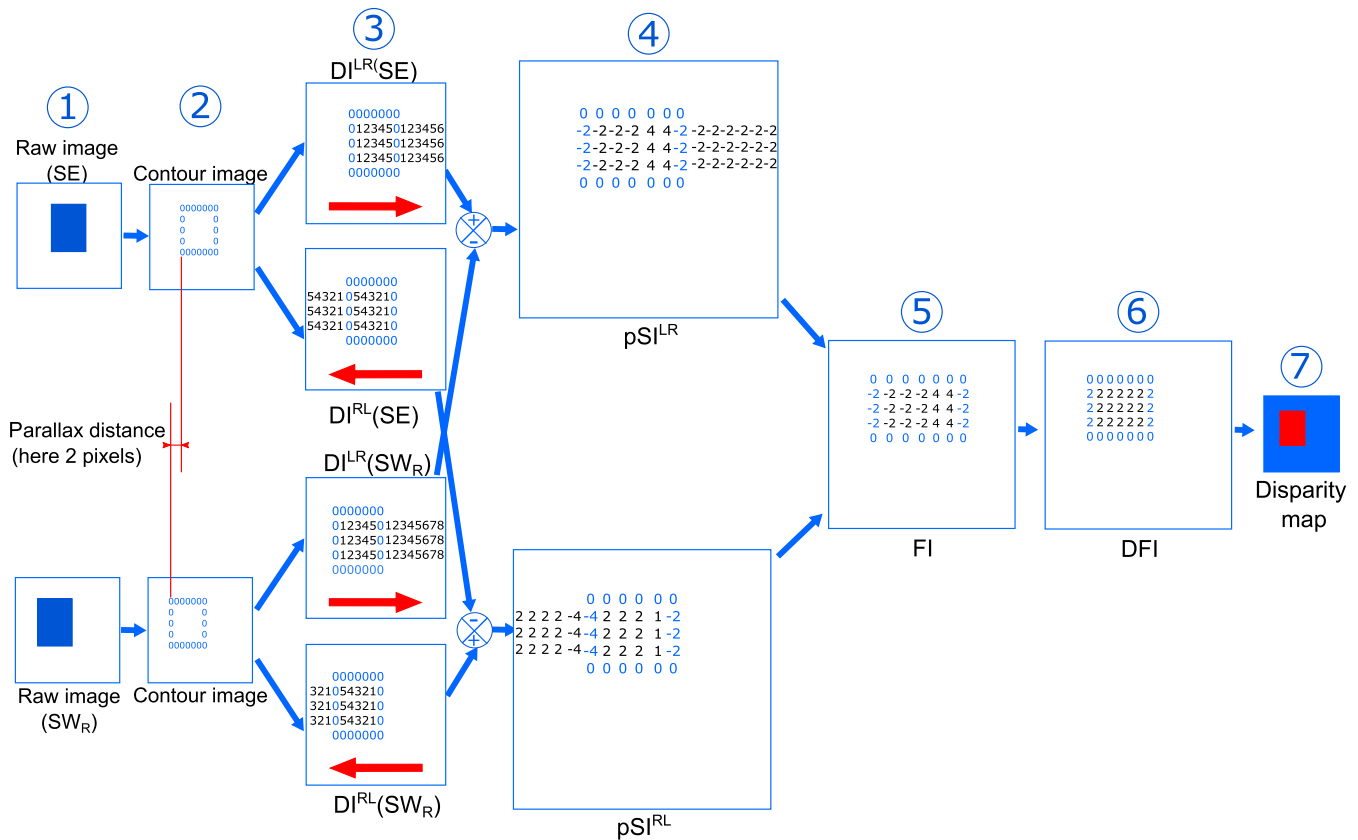
Fig. 7 Examples of pseudo-subtractions pSI^{LR}, pSI^{RL}, and FI for an object measuring $l = 8$ width and for a $d = 4$ disparity.

Fig. 8 Steps used for computing disparity map from SE and SWR subimages. 1: subimage acquisition; 2: binary contour extraction; 3: distance images computation according scanning direction; 4: pseudo-subtraction images computation; 5: fusion step; 6: image fusion decoding; and 7: final disparity map.
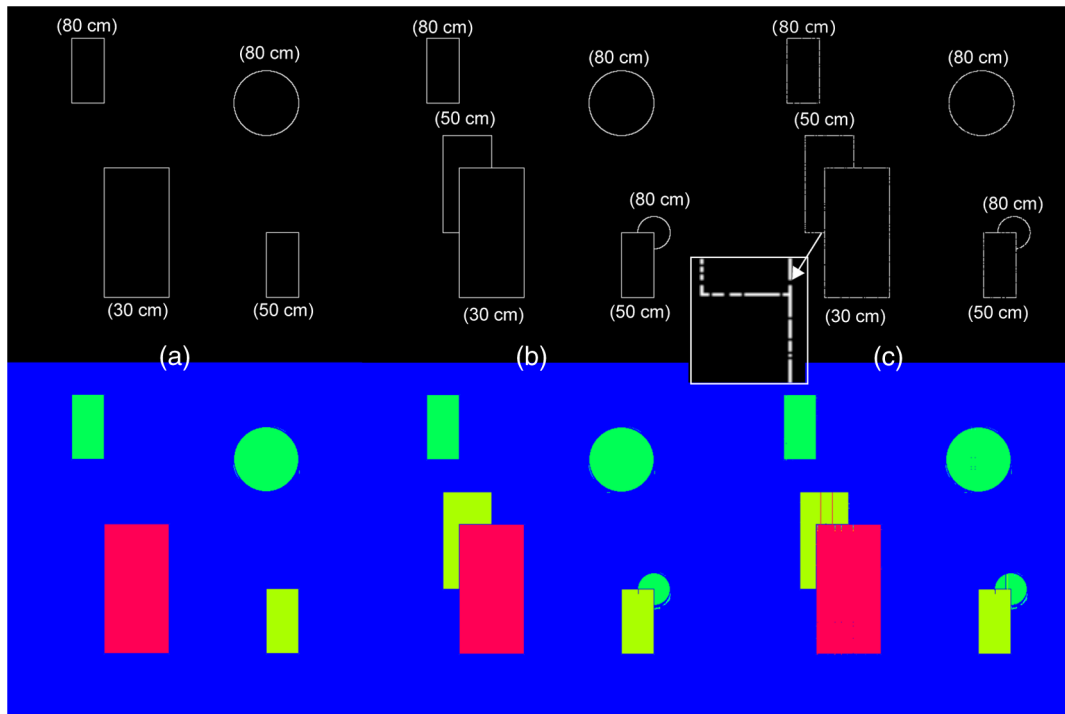

Fig. 9 Synthetic images (only subimage SE is shown) containing objects at different depths and corresponding depth maps: (a) four objects without superposition are placed in the scene; (b) some superposed objects are placed; and (c) contours in subimage are randomly degraded.

in experimental conditions. The map image is then computed with the merging process using here disparity images (SE, SW_R) and (SE, NE_R) as inputs. Final depth image still contains residual errors, but stays very close to the expected result and is suitable for most of 3-D inspection processes in industrial vision.

Instead of presenting experimental results in the form of depth images, we prefer defining the height images, which facilitates comparison with reference objects: height image $= Z_{A1} -$ depth image. Differences are just a translation of measurement values by the reference distance Z_{A1}. Figure 10 shows some typical height images computed on real scenes. We explore situations with objects having large uniform areas in natural lightning, for which standard matching methods often fail when no structured illumination is used. To do so, we have adapted the calibration distance Z_{A1} to the objects scale, as explained in Sec. 2.4. Heights measured for the four reference objects are then well recovered. One can however see some artifacts, which are still visible on the final depth map. The main characteristic of the proposed method is its ability to compute disparity map without requiring any matching. With a single-image sensor snapping simultaneously four views, the captured images present similar brightness and contrast. It could be expected that the edge detection provides same contours for the four views. In practice, due to the image sensor sampling, it is not always the case and some no-exact correspondences between detected contours are sometime encountered. Figure 11 presents an example of this situation, when no-exact correspondences between detected contours corrupt the depth map. Other artifacts could also be caused by the difference of point of views, resulting in occultation or hidden edges between the subimages. With our method, this kind of artifact is significantly smoothed by the merging process and is not the most frequently seen during our experiments.

Our approach for computing depth map is therefore validated by these synthetic and experimental results. This work should provide some new perspectives for establishing disparity maps without matching procedure, which is the main interest of the approach. The existing artifacts encountered in some cases should disappear or be attenuated by improving


(a)   (b)
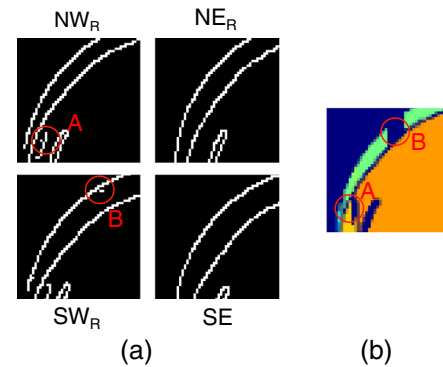
Fig. 11 Zooms on no-similar contours detection and corresponding artifacts on disparity maps: (a) four contours subimages; and (b) artifact areas where the contours are not identical.

and adapting an edge detection method for a multilens device.

4 Conclusions and Perspectives

We have described a multiview device considered as a multiview camera and used as a depth camera. This device can work for detecting objects to a depth of up to 2 m and could find interests for industrial vision. Main contributions consist first of an alternate approach for modeling and calibrating this device with variable homography, and second of an original and new approach for computing disparity map or depth images.

Variable homography is an alternate approach for modeling multiview systems. Main interest is to propose a rapid calibration procedure requiring only two acquisitions, without having to determine intrinsic parameters first. A comparison with the well-known triangulation method is performed, and we have demonstrated that the measurement uncertainties are then comparable, but calibration is easier in our case, especially if intrinsic parameters are not considered as identical for each subdevice. When optical distortions are significant, as for measurements performed at macroscopic scale, we have also proposed an improved calibration method,
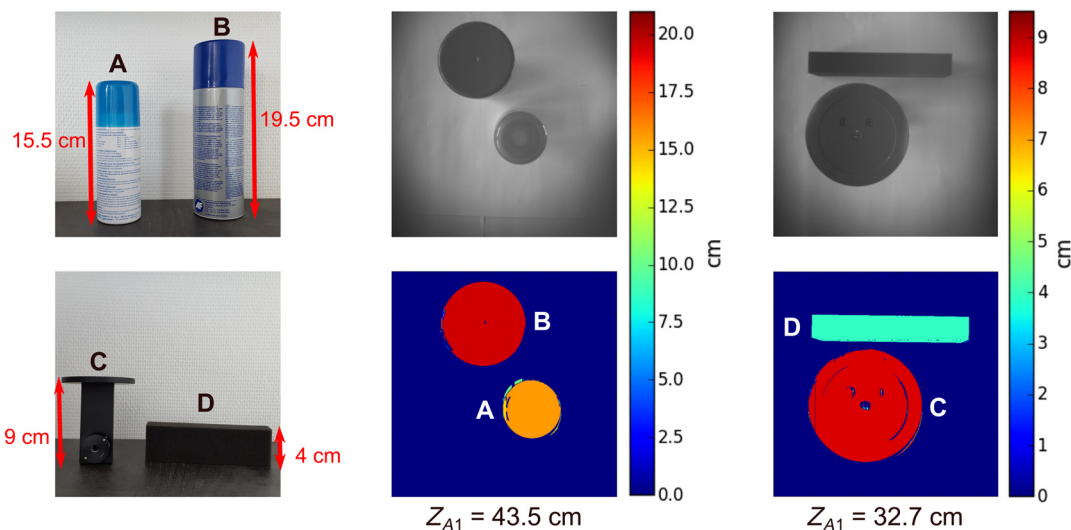
Fig. 10 Experimental results images (only subimage SE is shown) with four objects. Heights measured are: A: 15.6 cm; B: 19.4 cm; C: 8.7 cm; and D: 3.9 cm.

significantly reducing the measurement uncertainty. Calibration stays identical for normal and improved methods and always requires only two acquisitions. The principles developed with the variable homography method lead to use a reference homography called H_A, and the measurement is based on a disparity d defined as $d = H_B \cdot p_{2B} - H_A \cdot p_{2B}$.

In the second part of this paper, a new approach has been presented for computing disparity map, according to the definitions given previously. The major interest of this approach is to propose a new framework requiring no matching process defeated by uniform or poorly textured areas. This approach is well adapted for measuring height of objects placed under a camera for industrial vision control. By using contours, this method is efficient on flat and uniform objects in natural lightning. Our solution can be considered as an interpolating method of the disparity or depth information in uniform areas, giving a realistic rendering of simple objects. As the scene photometry is preserved, unlike measurements performed with active illumination, some other standard controls, as for example calipers, shape recognition, or barcode reading, can be done conjointly with 3-D measurement.

This work has validated the interest of our approach, and some interesting perspectives are envisaged. First, we project to extend the calibration for other models of multiviews cameras, such as the focused plenoptic[17] ones. A study of the best compromise between resolution, depth accuracy measurement, working distance, pixel size, and number of mini or microlenses should be performed. Second, we would like to improve the original method proposed for computing disparity map. In the future, we will focus on edge detection, in order to reduce artifacts and also extend our approach for natural and complex scenes.

References

1. R. Hartley, *Multiple View Geometry in Computer Vision*, 2nd ed., Cambridge University Press, Cambridge, UK (2003).
2. V. Vaish et al., "Using plane + parallax for calibrating dense camera arrays," in *Proc. CVPR*, pp. 2–9 (2004).
3. C. Birklbauer and O. Bimber, "Panorama light-field imaging: panorama light-field imaging," *Comput. Graphics Forum* **33**(2), 43–52 (2014).
4. E. H. Adelson and J. Y. A. Wang, "Single lens stereo with a plenoptic camera," *IEEE Trans. Pattern Anal. Mach. Intell.* **14**(2), 99–106 (1992).
5. A. Levin et al., "Image and depth from a conventional camera with a coded aperture," *ACM Trans. Graphics* **26**(3), 70 (2007).
6. D. Scharstein and R. Szeliski, "A taxonomy and evaluation of dense two-frame stereo correspondence algorithms," *Int. J. Comput. Vision* **47**, 7–42 (2002).
7. R. Szeliski, *Computer Vision*, Springer, London (2011).
8. V. Kolmogorov and R. Zabih, "Computing visual correspondence with occlusions using graph cuts," in *Conf. ICCV 2001*, pp. 508–515, IEEE Computer Society, Vancouver, British Columbia (2001).
9. Y.-C. Tseng, N. Chang, and T.-S. Chang, "Low memory cost block-based belief propagation for stereo correspondence," in *IEEE Int. Conf. Multimedia and Expo*, pp. 1415–1418, IEEE, Beijing, China (2007).
10. O. Veksler, "Stereo correspondence by dynamic programming on a tree," in *IEEE Conf. Computer Vision and Pattern Recognition (CVPR)*, pp. 384–390, IEEE, San Diego, California (2005).
11. Z. Zhang, "Camera calibration," Chapter 2 in *Emerging Topics in Computer Version*, G. Medioni and S. B. Kang, Eds., pp. 5–6, Prentice Hall PTR, Upper Saddle River, New Jersey (2005).
12. J. Xu et al., "Original method to compute epipoles using variable homography: application to measure emergent fibers on textile fabrics," *J. Electron. Imaging* **21**(2), 021103 (2012).
13. S. Zhang and M. Greenspan, "Variable homography compensation of parallax along mosaic seams," in *Image Analysis and Recognition*, M. Kamel and A. Campilho, Eds., Vol. **4633**, pp. 271–284, Springer, Berlin, Heidelberg (2007).
14. D. G. Dansereau, O. Pizarro, and S. B. Williams, "Decoding, calibration and rectification for lenselet-based plenoptic cameras," in *IEEE Conf. Computer Vision and Pattern Recognition*, pp. 1027–1034, IEEE, Portland, Oregon (2013).
15. Z. Zhang, "A flexible new technique for camera calibration," *IEEE Trans. Pattern Anal. Mach. Intell.* **22**(11), 1330–1334 (2000).
16. J. P. Barreto and K. Daniilidis, "Epipolar geometry of central projection systems using veronese maps," in *IEEE Computer Vision and Pattern Recognition*, pp. 1258–1265, IEEE, New York (2006).
17. C. Perwass and L. Wietzke, "Single lens 3D-camera with extended depth-of-field," *Proc. SPIE* **8291**, 829108 (2012).

Cecile Riou has been a PhD student at MIPS Laboratory, University of Haute Alsace (UHA), Mulhouse, France, since October 2014. She received her MS degree in optics, image, and vision from University Jean Monnet, Saint Etienne, France and an engineering degree from Telecom Saint-Etienne, Saint Etienne, France, in 2013. Her current research interests include 3-D vision, depth measurements, light-field cameras, and optical devices.

Bruno Colicchio received his PhD degree from the UHA, Mulhouse, France, in 2004 and worked during his thesis on deconvolution of 3-D fluorescence images. Since 2005, he has been assistant professor at IUT de Mulhouse and MIPS laboratory, and his research interests focus on image processing, fluorescence microscopy image deconvolution and optical diffraction tomography.

Jean Philippe Lauffenburger received his MSc and PhD degrees in electrical and control engineering from the UHA, Mulhouse, France, in 1998 and 2002, respectively. Since 2004, he has worked at the UHA in the MIPS laboratory, where he is currently an associate professor. His major research interests are data fusion, navigation, vision, joint association and tracking for intelligent transportation systems. He is a regular associate editor for IEEE and IFAC conferences.

Olivier Haeberlé is director of the MIPS Laboratory from UHA, France. Since September 2006, he has been a professor at IUT Mulhouse and Laboratory MIPS. From 1998 to 2006, he was assistant professor at IUT Mulhouse and Laboratory MIPS, UHA. In 1994, he received his PhD thesis from the Institute for Reference Material and Measurements (Belgium) and University Louis Pasteur (Strasbourg-France) for his works on "Electromagnetic radiation generated by relativistic electrons interacting with a diffraction grating."

Christophe Cudel received his PhD from the University of Reims Champagne Ardenne in 1995. He joined the UHA and the laboratory MIPS in 1997, first as assistant professor and now as professor. His research is focused on computer vision, eye-tracking, light-field and multi-view cameras. He teaches computer vision for industrial control, robotic and signal processing.